Title:

Attentional Information Routing in The Human Brain

Authors: Kianoush Banaie Boroujeni[1*], Randolph F. Helfrich[2], Ian C. Fiebelkorn[3], Nicole Bentley[4], Jack J. Lin[5], Robert T. Knight[6], Sabine Kastner[1,7]

Affiliations:

[1]Princeton Neuroscience Institute, Princeton University, Princeton, NJ 08544
[2]Hertie Institute for Clinical Brain Research, Center for Neurology, University Medical Center Tübingen, Tübingen, Germany.
[3]Department of Neuroscience and Del Monte Institute for Neuroscience, University of Rochester, Rochester, NY 14627, USA
[4]Department of Neurosurgery, University of Alabama at Birmingham, Birmingham, Alabama, USA
[5]Department of Neurology, University of California Davis, Davis, CA, USA
[6]Departments of Psychology and Neuroscience, University of California Berkeley, Berkeley, CA, USA
[7]Department of Psychology, Princeton University, Princeton, NJ 08544

*Corresponding author: Kianoush Banaie Boroujeni. Email: kb9590@princeton.edu

Abstract

Brain-wide communication supports behaviors that require coordination between sensory and associative regions. However, how large-scale brain networks route sensory information at fast timescales to guide upcoming actions remains unclear. Using spiking neural networks and human intracranial electrophysiology during spatial attention tasks, where participants detected a target at cued locations, we show that high-frequency activity bursts (HFAb) serve as information-carrying events, facilitating fast and long-range communications. HFAbs emerged as bouts of neural population spiking and were coordinated brain-wide through low-frequency rhythms. At

the network-level, HFAb coordination identified distinct cue- and target-activated subnetworks. HFAbs following the cue onset in cue-subnetworks predicted successful target detection and preceded the information in target-subnetworks following target onset. Our findings suggest HFAbs as a neural mechanism for fast brain-wide information routing that supports attentional performance.

Introduction

Prioritizing information from the external environment to guide ongoing behavior and upcoming actions requires coordination of neural activity on fast timescales across large-scale networks distributed across distant brain areas (*1–7*). This fast coordination allows information to be routed selectively from sensory to higher level executive brain networks (*8–12*). However, the mechanisms by which these fast neural dynamics emerge and enable information routing within large-scale brain networks are not well understood.

Investigating these questions at the network-level in the human brain is challenging due to spatial or temporal constraints of the techniques that have been employed. Studies examining network-level interactions have largely been based on connectivity maps derived from functional magnetic resonance imaging (fMRI) which has insufficient temporal resolution to capture fast routing dynamics (*13–17*). Studies using high temporal resolution methods such as electroencephalography (EEG) and magnetoencephalography (MEG), on the other hand, have limitations in spatial precision for measuring network dynamics (*18*, *19*). Lastly, single unit recordings provide both fine temporal and spatial signals but lack the broad coverage for addressing questions of brain-wide communication (*7*, *20*). In addition to these technical

challenges, cortex-wide neural dynamics have been mainly evaluated via spectral coherence between brain regions in low-frequency bands or coupling of high frequency activity to low frequency rhythms, which provides only an indirect measure of information routing and also cannot capture fast network interactions (*21–27*).

High frequency broadband activity (HFB) in human intracranial electroencephalography (iEEG), offers a unique opportunity to address these limitations by providing spatially localized and temporally precise data that can be instrumental to understanding fast cortical dynamics (*28*, *29*). These high-frequency activities can reflect different neural mechanisms depending on their recording source, including aggregated spiking activity of nearby neurons, neural post-synaptic activity, brain state shifting into spiking states, and spike current leakage to local field potentials (LFPs) (*30–33*). HFB has been widely reported to correlate with different cognitive functions, including attentional processes (*24*, *28*, *29*, *34–37*). In addition, HFBs show long-range phase synchronization with different frequency bands in the human brain, making them interesting candidates for studying fast and brain-wide communications (*22*, *24*, *38–40*). While previous research has highlighted the significant engagement of HFB in cognitive processes and its potential involvement in interareal communication through coupling to low-frequency rhythms, it remains unclear how HFB dynamics can inform about brain-wide communication and information routing at fast timescales.

Here, we established a novel method to investigate fast information routing within large-scale brain networks. We first detected transient high-frequency activity bursts (HFAbs) in human iEEG data from epilepsy patients performing spatial attention tasks. HFAbs were brain-wide

synchronized and linked to slow rhythms (4-25 Hz) and were found to occur more frequently during sensory and perceptual processing. HFAbs during cue processing and their local decoupling from low-frequency dynamics were associated with successful target detection. Network-level synchronization of HFAbs, identified functionally specialized brain subnetworks that activated in response to cues and targets. These subnetworks showed distinct topographical and temporal organization, with activity in cue-subnetworks preceding that in target-subnetworks. Using computational modeling, we further showed that HFAbs may reflect state transitions in neural populations into a coherent spiking activity state, characterized by bouts of elevated neuronal firing, which suggests HFAbs can serve as neural population-level signatures of information-encoding events. Our results demonstrate a novel mechanism for fast neural coordination in large-scale brain networks that supports attentional processes and facilitates information routing between functionally specialized brain subnetworks.

Results

HFA bursts predict behavioral accuracy

To examine neural mechanisms of fast information routing we used human iEEG data recorded from epilepsy patients to quantify high frequency activity dynamics. We analyzed data from two spatial attention tasks in which patients were cued either exogenously or endogenously to a spatial location to detect visual targets (**Fig. 1A**, **S1A**). Throughout the paper, the main figures mostly present results of experiment 1, while the results of experiment 2 are presented as supplementary information to indicate reproducibility and generalization across attention tasks (for brain heatmap plots, we combined both experiments to improve 3D rendering coverage).

98 In experiment 1, patients performed a spatial attention task as described in (*41*). Each trial
99 started with the presentation of two vertical or horizontal bar stimuli. Patients were instructed to
100 fixate their gaze at the center of the display. A transient spatial cue appeared at the end of one bar,
101 exogenously cueing an upcoming target location. Following a delay period, a target (i.e.,
102 luminance changes at perceptual threshold) appeared at the cued location or infrequently at equally
103 distant non-cued locations. Patients were required to respond if they detected the target (**Fig.**
104 **1A**). In experiment 2, patients were endogenously cued to a hemifield and expected to report a
105 target if it appeared in the cued hemifield (**Fig. S1A**, see **Methods,** and for more details see (*4*)).
106 First, we used an adaptive method (*7*) and detected reliable bursts of high frequency activity at
107 each electrode (HFAbs, 65-115 Hz, intermittent high amplitude oscillatory events lasting more
108 than 2.5 frequency cycles; **Fig. 1B**). The frequency band was selected based on average spectral
109 peaks observed across subjects (91.2 ± 20.9 Hz , n = 12, see **Methods** for further details). We then
110 calculated the HFAb density (number of HFAb events per unit of time) for each electrode to
111 examine their evoked response by different task epochs. HFAbs showed higher density averaged
112 across all electrodes in response to both cue and target (**Fig. 1B, S1B, S2A**). The HFAb activation
113 to targets was in most subjects negatively correlated with that to the cue, suggesting distinct groups
114 of electrodes processing cues and targets (4 of n = 7, Spearman correlation, $p<0.05$, R = -0.05 ±
115 0.07, mean ± standard error across all 7 participants, **Fig. 1D**). The topography of burst responses
116 to cues was largely confined to occipital and superior parietal regions (**Fig. 1E**), whereas those to
117 target responses were more widely distributed across different brain areas, including parietal,
118 motor, pre-motor, and lateral prefrontal cortices (**Fig. 1F**).
119 At the population level, HFAb responses to cues tended to be stronger in correct than in incorrect
120 trials, while the population-level burst responses to targets were significantly stronger for correct

121 detections (random permutation test. P<0.05, **Fig. 1G**, **S1C**). Cue responses (the average
122 normalized HFAb density within 500 ms following the cue-onset) were stronger in parietal areas,
123 whereas HFAb target-evoked responses were found to be stronger in motor/premotor areas for
124 correct, but not for missed trials (**Fig. 1H**, also see **Fig. S1E, S2C** for more individual examples).
125 Overall, cue responses were non-zero for correct hit and reject trials (Wilcoxon signed-rank test,
126 P<0.001), and they were also different in correct as compared to missed and false alarm trials
127 (Kruskal Wallis test, P=0.001, Dunn's test, P=0.008 and P=0.01, respectively; **Fig. 1I**). Target
128 responses were significantly different between correct hit and other outcome conditions (Kruskal
129 Wallis test, P<0.001, Dunn's test, P<0.001, **Fig. 1I**). We used Generalized Linear Mixed Effect
130 (GLME) models to examine the relationship between cue and target processing and outcome on a
131 trial-by-trial basis (see **Methods**). There was a main effect of outcome on both cue response (t=2.8,
132 P=0.005) and target response (GLME, t=15.2, P<0.001). Further, there was a main effect of cue
133 validity on the target response (GLME, t=4.7, P<0.001), and a main effect of the cue laterality on
134 the cue response (GLME, t=5.1, P<0.001). No significant main effect was observed for laterality
135 on target response (**Fig. S3A**, P=0.13), or validity on cue response (**Fig. S3B**, P=0.32, See **Fig.**
136 **S3C,D** for the effect of laterality and cue validity on cue and target response in experiment 2, as
137 well as **Fig. S3E,F** for the temporal profiles of HFAbs around cue and target onsets in both
138 experiments).
139 Next, we examined whether the burst density of electrodes that showed significant activation in
140 response to cues (Cue+ electrodes, see **Methods**) predicted whether participants would
141 successfully complete a trial (correct hits and correct rejections). We trained a classifier on the
142 burst density using a sliding window of 350 ms around the cue onset. In Cue+ electrodes and
143 within 500 ms after the cue onset, the burst density predicted higher than the baseline level and the

144 chance level if the trial would be executed correctly (binomial test, FDR corrected for dependent
145 samples, P<0.05, **Fig. 1L, S3G**). This prediction was consistent across both experiments (**Fig.**
146 **S3H**) and was not dependent on an individual subject (**Fig. S3I**).
147 These findings indicate that HFAbs occur more frequently in response to sensory cues and targets,
148 while exhibiting distinct spatial profiles across the brain. The cue response was predominantly
149 observed in occipital and parietal regions and predicted performance accuracy following the cue-
150 onset on a trial-by-trial basis. These results suggest a potential role for HFAbs in encoding and
151 routing spatially relevant sensory information for subsequent target detection.
152
153 **HFA bursts are synchronized in cortical networks**
154 High frequency activity dynamics in brain networks are shown to be organized by low-frequency
155 rhythms, involving in different cognitive processes (*22*). Thus, we examined if HFAbs are
156 coordinated with slower rhythms of local population activity, and if behavioral variables affect
157 these local coordination patterns. For each electrode, we extracted the LFP around the HFAb
158 centers and measured the HFAb-triggered LFP average, as well as phase locking value (PLV) of
159 HFAbs to the low frequency dynamics of LFP. The HFAb-triggered LFP showed consistent
160 evoked potentials with low frequency side-lobes across all subjects (**Fig. 2A**). HFAbs triggered
161 spectral peaks (**Fig. 2B**, top) and phase locking peaks (**Fig. 2B**, bottom) predominantly in the theta
162 frequency band (4-8 Hz), as well as in alpha and beta frequency bands (8-14 Hz and 15-25 Hz,
163 respectively). The phase locking of HFAbs to the local low-frequency field dynamics was evident
164 in most electrodes and across all subjects (**Fig. 2C,** 9 ± 0.24 Hz**,** significant peaks are shown with
165 black dots; see **Fig. 2D, S4C** for examples of individual electrodes showing phase distributions of
166 HFAbs locked to one or more frequency bands, also see **Fig. S4A,B** for a topographic

167 representation of the frequency of phase locking peaks at the group average and individual subject
168 levels).
169 We next examined whether sensory cues or target processing affected HFAb phase locking to
170 the local population. Overall, HFAbs showed a transient decrease in their local phase locking to
171 low-frequency rhythms relative to the baseline following cue and target onsets (**Fig. 2E**). This
172 decrease in phase locking value is referred to as *decoupling*. HFAbs decoupled from the theta/alpha
173 and beta frequency bands after the cue onset and after the target onset (**Fig. 2F, S4D,**
174 randomization test, $P < 0.05$, FDR corrected for dependent samples). This decoupling was not
175 induced by event-triggered potentials (**Fig. S4E**, see **Methods**). Also HFAb coupling strength
176 changed only in correct trials, but not in incorrect trials (**Fig. 2G,H,** the number of bursts was
177 controlled across trial conditions, see **Methods**, see **Fig. S4F** for individual examples). The
178 decoupling was consistent across most participants in both tasks at the network level (**Fig. 2I,**
179 **S4G,H**, 4 and 8 of the $n = 12$ subjects showed significant decoupling at the network level after the
180 cue and target onset, respectively; Wilcoxon rank-sum test, $P<0.05$).
181 We then examined whether alterations in HFAb coupling to low frequencies were related to HFAb
182 activation profiles in response to cues and targets. We calculated correlations between coupling
183 ratios and burst density for each subject (a coupling ratio measured changes in HFAb coupling to
184 low frequencies after cues or targets relative to the baseline within 1000 ms before the cue and
185 target onset, see **Methods**). The coupling ratio at target and cue onsets was negatively correlated
186 with burst density for most participants (**Fig. 2J, S4I**, 8 of $n = 12$ subjects showed a significant
187 negative correlation, Spearman correlation, $P<0.05$). Burst density and coupling ratio were
188 correlated within the same event, indicating that coupling was not dependent upon burst activation
189 to the other events (**Fig. 2J**, Fisher test, $P<0.001$). Overall, the dynamic coupling of HFAbs to

local low-frequency activity suggests that while these HFAbs are primarily organized by local dynamics, they can decouple from their local network when receiving and processing sensory information as well as during perceptual processing and decision making.

HFAbs were coordinated brain-wide and their baseline synchronization identified functionally specialized subnetworks

We found that HFAbs evoked by cue and target demonstrated different topography. In addition, the processing of cues and targets involved the decoupling of HFAbs from local low-frequency dynamics. These observations suggest the possibility that brain networks may coordinate at a large scale when processing these events, rather than processing them locally. Thus, we asked whether the brain-wide network could be organized into distinct functionally specialized subnetworks, each characterized by unique high frequency coordination patterns. To avoid stimulus-driven coordination in the network, we only considered burst events outside of the cue/delay and target/response periods. To examine this coordination, we measured the power of high frequency broadband activity (65-175 Hz, HFB, to capture broader spectral contents) in one electrode aligned to the center of HFAb events in another electrode (HFAb-triggered HFB). HFAb-triggered HFB between most channels revealed activity coordination in high frequency bands (**Fig. 3A**). The HFAb coordination between electrodes was organized through a low frequency rhythm showing spectral peaks mostly in theta band (4-8 Hz) among the majority of electrodes (**Fig. 3B**, top) and consistent across all subjects (**Fig. 3B**, bottom, similar patterns were observed in experiment 2, **Fig. S5A,B**). HFAb coordination strength (the sharpness of HFAb-triggered HFB) was inversely related to distance between electrodes, with closer sites showing stronger coordination (**Fig. 3C**,

212 **S5E**, Spearman correlation between coordination kurtosis and distance between electrodes, R = -
213 0.25, P<0.001).
214 To extract prominent temporal features of the high frequency coordination in the network, we
215 reduced dimensionality of HFAb-triggered HFB by Principal Component Analysis (PCA),
216 considering each electrode pair as a single dimension. All subjects showed zero-lag synchronized
217 and near-symmetric distributions of high frequency activity in their first component, explaining
218 on average more than 20% of the total variance (**Fig. 3D, Fig. S5D,E**). We projected HFAb
219 coordination between electrode pairs onto their PC space and calculated the scores for all electrode
220 pairs on the synchronized PC (**Fig. S5F**, PC1). Using a correlation-based K-means clustering
221 technique, we identified electrodes that were consistently grouped together based on their score on
222 this synchronized component (**Fig. S5F,** see **Methods**). While the clustering algorithm generates
223 most stable clusters for each cluster number (K = 2-8, see **Fig. S6A** and **S7A** for individual
224 examples), we defined a series of accuracy metrics to find a balance between the highest number
225 of reliable clusters and the highest degree of accuracy in each subject (**Fig. S6B,C** and **Fig. S7B,C,**
226 see **Methods**). An example of clustering for one subject with eight optimal clusters is shown (**Fig.**
227 **3E,** also see **Fig. S8** for topographical organizations of clusters in different subjects).
228 Next, we investigated whether these clusters were functionally specialized. In most subjects,
229 clusters showed distinct activation profiles following cue and target onsets (**Fig. 3G,** see **Fig. S9**
230 for an example of activation profiles for different cluster numbers, also see **Fig. S6D** and **Fig. S7D**
231 for additional examples). We labeled clusters that were significantly activated by cue and target
232 events as *cue* and *target-subnetworks*, respectively (**Fig. 3**h; Wilcoxon signed-rank test, P<0.05;
233 FDR corrected for dependent sample). Across both tasks, 6 out of =12 subjects showed stable cue-
234 subnetworks, and 10 showed stable target networks, respectively. Cue-subnetworks were

235 predominantly located in occipital and parietal cortices, while target-subnetworks were more
236 widely distributed across different brain areas including parietal, motor, premotor, and lateral
237 prefrontal cortices (**Fig. 3H**).
238 We examined if stable cue and target-subnetworks could predict trial outcomes. A classifier was
239 trained on the HFAb density of cue and target-subnetworks in sliding windows around the cue
240 onset to predict trial outcomes. The HFAb density within 98-374 ms after sensory cues predicted
241 successful detection of upcoming targets better than both baseline and chance level (binomial test,
242 $P<0.001$, FDR corrected for dependent samples). This prediction was only true for the cue-
243 subnetwork (**Fig. 3I**) and was not driven by a single subject (see **Fig. S10** for more details on the
244 classifier results in both experiments). As a control analysis, we re-referenced the datasets from
245 common average referencing to local composite referencing (LCR, each electrode was referenced
246 to its nearest neighbors, see **Methods**), which did not alter any of the main results.
247 Together, these findings suggest that large-scale brain networks can be divided into subnetworks
248 with distinct HFAb temporal dynamics. These subnetworks are further characterized with their
249 unique responses to sensory cues and targets, with the cue-activated subnetworks containing
250 information predictive of performance accuracy following cue onsets.
251

252 **Cue-subnetworks precede the information flow triggered by targets within target-**
253 **subnetworks**

254 Our observation that cue-subnetworks responses predict performance accuracy led to a key
255 question: whether cue-subnetworks routed information to target-subnetworks during target
256 processing. To address this question, we examined the information flow between cue and target-
257 subnetworks. We only considered subjects that showed both stable cue and target-subnetworks (3

258 subjects in each experiment). We used two different approaches. First, we quantified whether
259 HFAbs exhibited any temporally ordered activity pattern during the target-to-response period
260 between cue and target-subnetworks. When we averaged the time-lags between cue and target-
261 subnetworks over different cluster numbers, we observed that the HFAbs in occipital, posterior
262 parietal, and prefrontal areas led over motor/premotor areas during target processing (**Fig. 4A**, see
263 **Fig. S11A** for more examples). Individual subjects showed stronger HFB in target-subnetworks
264 within 150 ms after HFAbs in cue-subnetworks (**Fig. 4B, Fig. S11B,** Wilcoxon rank-sum test,
265 $p<0.05$, the opposite pattern was observed in the other direction). On average, HFAbs in cue-
266 subnetworks led the activity of target-subnetworks while target-subnetworks lagged cue-
267 subnetworks during the target processing period (within 150 ms around the HFAb-triggered HFB,
268 Wilcoxon rank-sum test, $p<0.001$, **Fig. 4C).** For comparison, no lead-lag patterns were observed
269 between cue and target-subnetworks during the cue-to-target interval **(**$P=0.44$, n.s., **Fig. S11C).**
270 We quantified the peak of these lead-lag relationships for individual subjects. The HFB in target-
271 subnetworks showed an activity peak following HFAbs in cue-subnetworks, while the peak of
272 HFB in cue-subnetworks preceded HFAbs in target-subnetworks (**Fig. 4D**, Wilcoxon rank-sum
273 test, $p<0.05$, 16 ± 7 ms; $n = 6$**).**
274
275 Next, we used delayed mutual information (DMI) to further quantify how information was
276 directionally coupled between cue and target-subnetworks. DMI can inform about (i) when cue
277 and target-subnetworks shared the most information relative to target onset, and (ii) the specific
278 time-lags at which these two subnetworks showed maximum inter-predictability (see **Fig. 4E** for
279 an individual example).

The DMI between cue and target-subnetworks showed a peak up to 500 ms after target onset (**Fig. 4F,** 275 ± 22 ms; n = 6). Time-lag distributions of the maximum DMI between cue and target-subnetworks showed that cue-subnetworks preceded the information in target-subnetworks during the target processing period (Wilcoxon signed-rank test, P<0.001; 67 ± 16ms, n = 6, **Fig. 4F**). This pattern was consistent for individual subjects (**Fig. 4E,G**, see **Fig. S11D** for more examples) as well as on an average group level (**Fig. 4F**). The information precession in cue-subnetworks over target-subnetworks was only evident after the target onset (no significant time-lag was observed around the cue onset, showing this effect is not a reflection of visual hierarchy activation **Fig. S11E**), and limited to trials with a valid sensory cue (the target appeared as instructed by the visual cue, **Fig. 4G**). Overall, these results indicate that information processing in cue-subnetworks precedes that in target-subnetworks when the cue poses valid information about the target.

Computational modeling of HFAbs through spiking neural networks

We used spiking neural networks to investigate potential neural mechanisms underlying HFAbs in iEEG signals. We simulated two interconnected networks of spiking neurons (*42*), each consisting of 1000 neurons, including an average of ~80% excitatory pyramidal neurons and ~20% inhibitory interneurons with different subtypes (**Fig. 5A, S12A,** see **Methods**). Each network was fed by external input currents primarily to the excitatory population.

We implemented two recording sites on top of each network measuring electrical field dynamics of postsynaptic and transmembrane potentials from all neurons in that network (**Fig. 5A)**. A non-ohmic filter was used to attenuate higher frequencies in the iEEG signal (**Fig. 5B**, **S12B,C** see **Methods**). The recorded iEEG signal showed low-frequency spectral peaks reflecting the resonance frequency of each network (*7*) and high frequency spectral peaks in the range of 65-115

Hz (**Fig. 5C**). Similar to our experimental results, we detected HFAbs as transient oscillatory events of high amplitude 65-115Hz at each recording site (**Fig. 5D**).

To investigate the neural mechanisms underlying these HFAbs, we calculated the spike density for the population of neurons, and the HFAb density (number of bursts per unit of time) from each recording site. Burst density was significantly correlated with spike density as compared to bursts with random timings (randomization test, $P<0.05$, **Fig. 5D**). This was further quantified by feeding the network different levels of external current coherence (**Fig. S12C)**. Increasing the input coherence to the network showed a linear increase in correlation between the HFAb density and the spike density (Spearman correlation, $R=0.87$, $P<0.001$, **Fig. 5E**). This observation is consistent with our experimental findings that HFAbs are evoked in response to cues and targets, suggesting that they may reflect large-scale information-carrying events emerging from transiently elevated excitation in local networks of neurons.

Next, we asked how HFAbs coordinate with slower rhythms locally. We measured HFAb-triggered LFPs at each recording site, which showed an average evoked response with low-frequency sidelobes (**Fig. 5F**). The HFAb-triggered LFP spectrum showed peaks in low frequencies as well as the burst frequency band (**Fig. 5G**). The cross-spectral correlation was dependent on synaptic time constants, external input strength, neural connectivity strength, and coherent input consistency (**Fig. 5G**). In addition to the spectral correlation between HFAbs and the LFP, HFAbs also showed phase locking to different frequencies in the theta, alpha and beta frequency bands (4-25 Hz, **Fig. 5H**). These results are consistent with the prominent local cross-spectral coupling observed in our experimental data, suggesting local neural network mechanisms underlying the coupling of high- and low-frequency dynamics.

We also tested for possible network mechanisms underlying the decoupling following cue and target processing. We modeled this scenario through feedforward networks and measured the time-resolved PLV for both networks after feeding one with a brief input pulse (~50% of the population simultaneously received in-phase inputs simulating an external stimuli; **Fig. 5I, S12E,F**). The external impulse desynchronized both networks, resulting in a transient decoupling of HFAb from low-frequency activity as compared to the baseline (Wilcoxon rank-sum test, $P<0.001$, **Fig. 5I, S12G,H**). This confirmed that desynchronization was not due to lower burst rate (**Fig. S12I)**.

Lastly, we examined how HFAbs might be coordinated between distributed networks of neural populations. Similar to our experimental data, we measured HFAb-triggered HFB by aligning HFB power in one network to HFAb times in the other network. HFAbs showed different rhythmically organized coordination patterns between networks depending on inter-network connectivity and external inputs. Reciprocally connected networks and networks with correlated external inputs showed synchronized high frequency activity (**Fig. 5J**), while feedforward networks showed a lead-lag pattern within 150 ms following HFAbs (Wilcoxon rank-sum test, $P<0.001$, **Fig. 5K**). In addition to the internally generated rhythmic structure of HFAbs between networks, external inputs may also contribute to these rhythmic coordination patterns. A rhythmic input to either or both networks entrained its rhythm in the coordination between the two networks (Spearman correlation, $R = 0.83$, $P < 0.001$, **Fig. 5L,M**).

In sum, our modeling results suggest that HFAbs reflect a state transition in neural populations into a coherent spiking activity state. By default, these HFAbs are phase locked to low frequency activity, but decouple when transient inputs interfere with internally generated network states. HFAbs are coordinated across interconnected networks or networks with correlated external drives.

Discussion

Here we present a novel framework for understanding the mechanisms underlying large-scale information routing in brain networks at fast timescales. We identified brain subnetworks characterized by similar high-frequency activity coordination patterns, which tracked the encoding and transfer of spatially relevant sensory cue information within large-scale brain networks. Using computational modeling, we showed that HFAbs can emerge as bouts of elevated excitatory drive to local networks, which may serve as fast communication units across the brain. These burst events were synchronized across distributed brain networks in iEEG data, and their network-level synchronization patterns revealed functionally specialized subnetworks for processing cues and targets. HFAbs in cue-subnetworks predicted successful target detections on a trial-by-trial basis and preceded the activity of target-subnetworks during target processing. These findings demonstrate, to our knowledge, for the first time that high-frequency activities can be involved in both forming a brain-wide representation of sensory inputs and facilitating the communication of these sensory signals to associative brain networks for detecting upcoming targets and decision-making processes.

High-frequency activities (HFB or high gamma) have been widely observed in human intracranial recordings and are associated with a wide range of cognitive and circuit functions (*22*, *24*, *26*, *28*, *29*, *37*, *38*). Our results align with these previous studies, showing prevalent high-frequency activity in human iEEG signals. However, instead of continuous measures, we characterized these activities as discrete burst events that may reflect coherent bouts of excitation in neural populations, as previously shown in monkey electrophysiology and modeling studies as an important mechanism in facilitating information routing between distant brain areas (*7*, *43*, *44*).

This discrete description of high-frequency dynamics is also supported by previous research in animal models emphasizing their circuit-level origins and their essential roles in long range communications (*43*, *45–49*). In addition, while cross-frequency coupling have typically been observed between high-frequency amplitude and low-frequency phase in theta and alpha bands (*21*, *22*, *24*, *41*), our discrete quantification of these high-frequencies enabled the study to explore their interactions with a broader frequency range (including low and high beta bands, 15-35 Hz). This unique characterization of high-frequency activities opens new avenues for understanding fast and long-range information routing and network-level communication mechanisms in different cognitive processes.

One of the main findings of our study was revealing the synchronized inter-regional temporal structure of high-frequency coordination through HFAbs. We found that the most prominent pattern of high frequency dynamics in the brain network was zero-lag amplitude synchronization (**Fig. 3D**). This long-range synchronization of HFAbs is consistent with previous studies showing phase locking of high frequency dynamics in brain networks (*38–40*). Zero-lag synchronization patterns in cortical networks are thought to enhance large-scale information processing and facilitate representational states of sensory information in the brain (*2*, *50–52*). While our results cannot directly identify the origins of these synchronized interactions, two different scenarios might be involved. One potential mechanism relies on subcortical areas (*53–57*), particularly the higher-order thalamic nuclei (*53*, *58–61*). Our modeling suggested that long-range synchronization might result from correlated inputs to two distinct networks of neurons (**Fig. 5L**). Such correlated inputs, if originating from subcortical structures such as higher-order thalamic nuclei, can facilitate

393 the long-range synchronizations between separate or weakly connected cortical areas (*53*, *62*).
394 Another mechanism depends on long-range intracortical interactions. We found that cortical
395 synchronization was largely between areas with similar activation profiles during cognitive
396 functions and spatially neighboring regions (**Fig. 3, S8**). Additionally, our modeling suggested that
397 reciprocally connected networks with similar connectivity strength can result in synchronized
398 dynamics (**Fig. 5J**). This zero-lag synchronization induced by reciprocal connections has been
399 observed experimentally in long-range neuronal interactions (*50*, *51*) as well as in network
400 modeling (*63*). Recent findings in mice support this idea by showing that deep layer 6b neurons,
401 which are recipient of long-range cortical projection neurons (*64*), are involved in brain state
402 shifting into a spiking state, and strong high gamma activity in brain networks (*33*). While our
403 modeling and empirical results can support either of these mechanisms, future studies need to
404 explore the extent to which cortico-cortical versus thalamocortical interactions drive and influence
405 this high frequency synchronization in large-scale cortical networks.

406 We further showed that network-level baseline synchronization fingerprints of high-frequency
407 dynamics outside of task events can be used to identify distinct functional brain subnetworks
408 through a novel clustering framework. While the baseline state did not contain cue or target
409 processing periods, it could identify subnetworks with unique activation patterns in response to
410 those behavioral events (**Fig. 3**). Our findings are consistent with several fMRI studies suggesting
411 functional brain networks are continuously active, even during resting states (*65*, *66*). However,
412 using methods with high spatial and temporal resolution we can understand both variabilities
413 within each subnetwork, as well as their dynamic interactions, which may not readily be resolved
414 by imaging techniques. Our results revealed that brain subnetworks, identified by their network
415 synchronization, exhibit lead-lag interactions during behavioral events that involved information

416 routing. Specifically, cue-subnetworks lagged target-subnetworks during target presentation when
417 spatial cues provided relevant information about target locations (**Fig. 4**). These observations are
418 particularly unique as they bridge the gap between studies focusing on local and cross-regional
419 mechanisms of fast information routing (*7*, *26*, *43*, *46*, *48*, *58*, *67*) and those examining
420 communication in large-scale brain networks beyond pairwise interactions (*17*, *68*, *69*).
421
422 Lastly, another key and rare finding of our study is the coupling dynamics of HFAbs and local
423 low-frequency activities. We found that the phase-locking of HFAbs to low-frequency dynamics
424 can occur with random external input patterns in the modeling, and this is a widespread
425 phenomenon in iEEG signals, consistent with previous studies (*22*, *70*, *71*). However, our findings
426 further suggest that HFAbs transiently decouple from the phase of local low-frequency activities
427 in response to cue and target events (**Fig. 2**). Our modeling supports this observation, showing that
428 transient inputs, whether directly fed into a network (e.g., a visually evoked response from
429 subcortical structures) or indirectly through a feedforward structure, can interrupt the default state
430 coupling of HFAbs to low frequencies (**Fig. 5I**). Network interferences, characterized by brief and
431 strong responses, can temporarily induce local cross-frequency decoupling possibly by increasing
432 response heterogeneity and disrupting the timing of inhibitory and excitatory neuron activation
433 (*72*, *73*). This desynchronization can facilitate cognitive processes like selective attention,
434 perception, and memory retrieval by enriching represented information and suppressing internally
435 regulated activity states (*72*, *74–78*). We observed that HFAb decoupling from low-frequency
436 dynamics, accompanied by increased HFAb density following cue and target events, resembling a
437 desynchronized up-state in cortical networks. Importantly, this decoupling was more pronounced
438 in correct trials during both cue and target processing, further supporting the role of

desynchronization in facilitating accurate cognitive performance (**Fig. 2H**). Future studies need to investigate the origins of these coupling dynamics, their implications in other cognitive domains, and their causal contributions to local and brain-wide information processing.

In summary, our study provides a systematic approach to understanding large-scale cortical communications, showing that HFAbs act as fast communication units in the brain, supporting long-range information processing, facilitating attentional information routing, and identifying distinct and functionally specialized brain subnetworks.

Acknowledgments

This work was supported by the C.V. Starr Fellowship (KBB), German Research Foundation, Emmy Noether Program (DFG HE8329/2-1; RFH), NINDS (R01NS021135; RTK), and NEI (2R01EY017699; SK), NIMH (2R01MH064043, P50MH109429; SK). The funders had no role in study design, data collection and analysis, the decision to publish, or the preparation of this manuscript.

Author Contributions

Conceptualization, K.B.B. and S.K.; Methodology, K.B.B.; Formal Analysis, K.B.B.; Investigation, R.F.H., and J.J.L.; Software, R.F.H. and I.C.F.; Visualization, K.B.B; Writing – Original Draft, K.B.B.; Writing – Review & Editing, K.B.B., R.F.H., N.B., R.T.K., and S.K..; Supervision, S.K.

Data and code accessibility

Custom programming code for analysis and modeling is available upon publication and will be deposited in an online directory.

Competing Interest: The authors declare no competing interests.

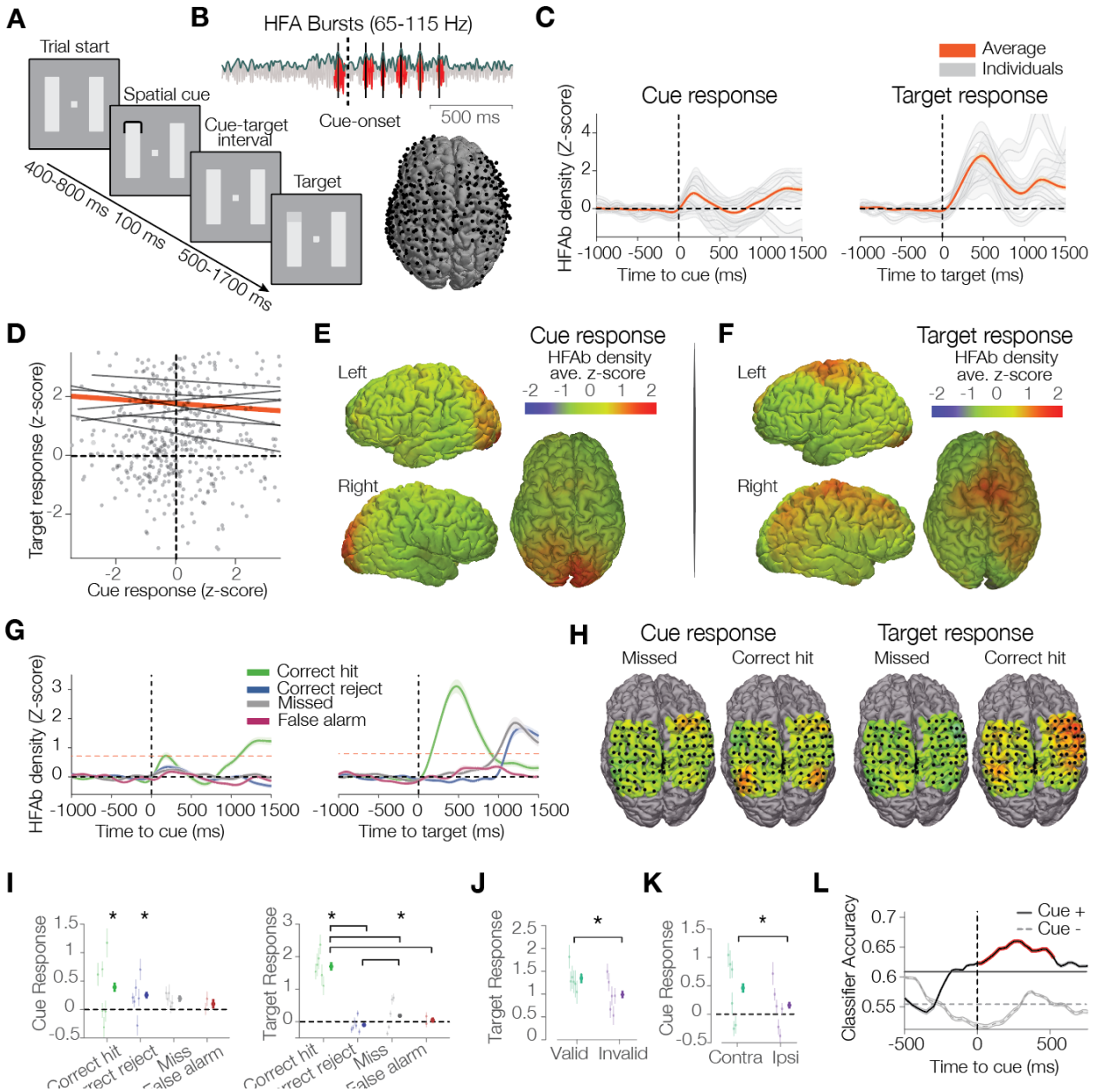

Fig. 1. HFAb activation profile predicts behavioral outcome on a trial-by-trial basis. (A) A schematic of experiment 1 task outline. Two bars appear on the screen. A transient cue informs the subject of the most probable location of an upcoming target. A target at perceptual threshold contrast change appears at a cued or infrequently at an equidistant uncued location after a variable interval. Subjects report the change detection. (**B**) An example trial of detected transient high-frequency bursts (HFAbs, shown in red) around the cue onset. The brain shows localization of electrodes across all subjects. (**C**) Normalized HFAb density profiles for individual subjects and averaged across participants aligned to the cue (left) and target onset (right). (**D**) Correlation of HFAb responses evoked by cue and target onset (each point represents one electrode, each line represents regression for one subject, the orange line shows regression across all electrodes). (**E, F**) Group average heatmap 3D rendering of HFAb responses to (**E**) cues and (**F**) targets. (**G**) Activation profiles of HFAbs grouped by trial outcome. The dashed lines indicate the significance level ($P<0.05$, permutation test). (**H**) An individual subject example of HFAb responses to cue and

target within 500 ms and 700 ms after the cue and target onset, respectively, for correct and incorrect trials (black circles indicate electrode locations). (**I**) HFAb responses to cues (left) and targets (right) grouped by trial outcome. (**J**) HFAb responses to targets for valid and invalid cue conditions. (**K**) HFAb responses to cues ipsi- and contra-lateral to electrodes. (Each line represents one subject, with thick lines showing group average, horizontal lines showing significant differences between groups, and asterisks denoting non-zero responses). (**L**) Classifier accuracy in predicting trial outcome based on HFAb density around the cue onset for cue responsive electrodes and cue unresponsive electrodes (error bars indicate standard error of the mean across all realizations and cross validations). Red lines indicate significantly higher prediction accuracy than baseline and chance levels ($P<0.05$, binomial test, FDR corrected for dependent samples).

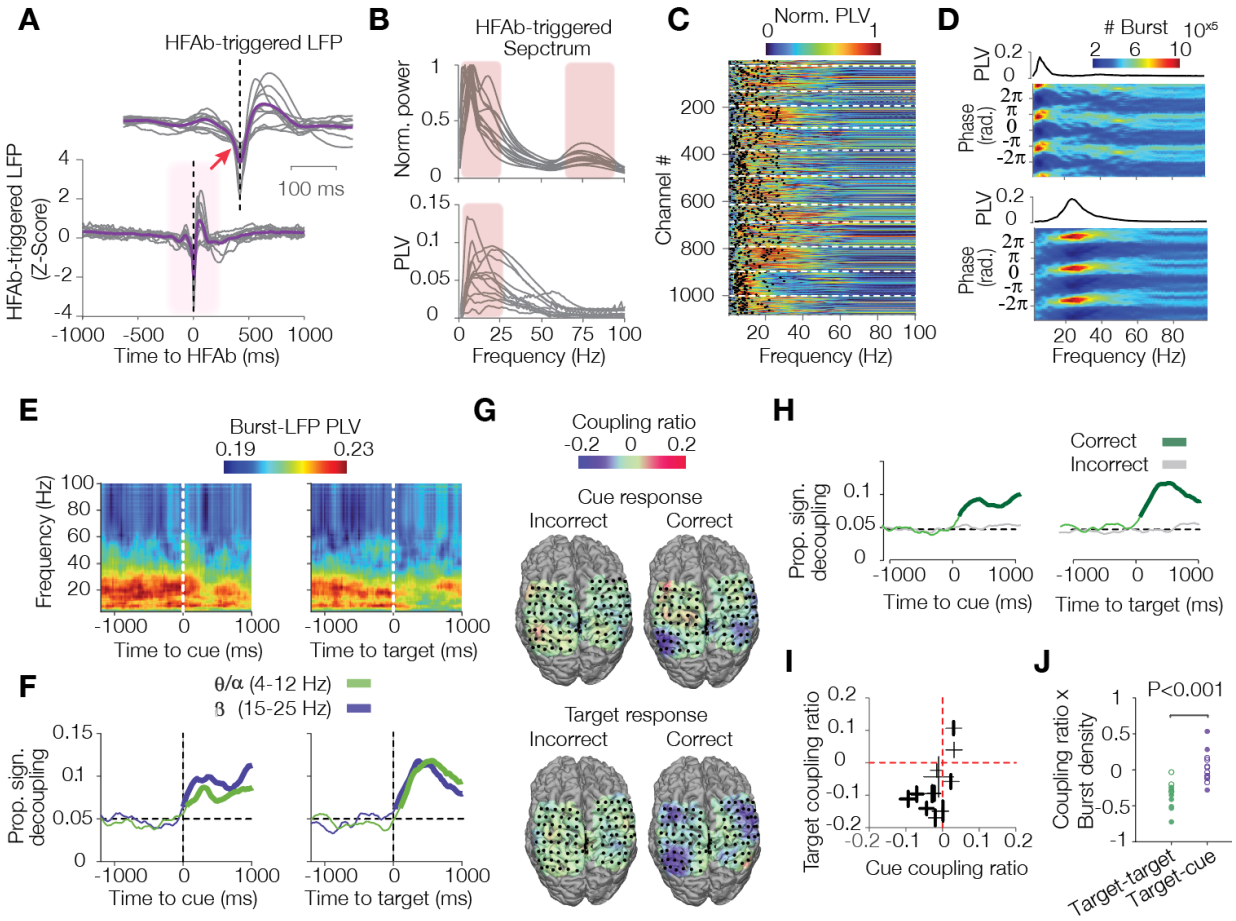

Fig. 2. HFAbs dynamically phase lock to low frequency LFPs and decouple transiently after cue and target onsets. (**A**) HFAb-triggered LFP averages across all electrodes for individual subjects (gray lines) and across all individuals (purple line). (**B**) HFAb-triggered LFP spectrum (top) and phase locking values (PLV, bottom) across all electrodes (each line represents one subject). **(C)** PLVs for individual electrodes (each row)**.** Black circles indicate the maximum peak of PLV for each electrode, and white dashed lines delineate results from individual subjects. **(D)** Example of phase-frequency distribution of HFAbs for an electrode with theta phase locking (top) and beta phase locking (bottom). (**E**) Time-resolved PLV analysis averaged across all subjects aligned to cue (left) and target (right) onsets. (**F**) The proportion of time points where phase locking dropped significantly below the baseline averaged across all electrodes (P<0.05, random permutation test; thick lines indicate segments significantly different from the chance level, P<0.05, binomial test, FDR corrected for dependent samples; see **Methods**). (**G**) An individual brain heatmap example showing coupling ratio between HFAb and low frequency (4-25 Hz) LFP after cue (top) and target onsets (bottom) for correct and incorrect trials. (**H**) Similar to F, proportion of time points with significant decoupling from low frequency LFPs (4-25 Hz) after cue and target onsets for correct and incorrect trials. (**I**) Average cue-target coupling ratios across electrodes for individual subjects. Each line shows the median ± standard error, thick lines indicate significant non-zero coupling ratios (P<0.05, Wilcoxon test). (**J**) Correlation between burst density within 500 ms after the target onset and coupling ratios for cue (purple) and target (green) processing. Circles indicate individual subjects, and filled circles indicate significant correlations. The horizontal line indicates significant differences between the two conditions (P<0.001, Wilcoxon test).

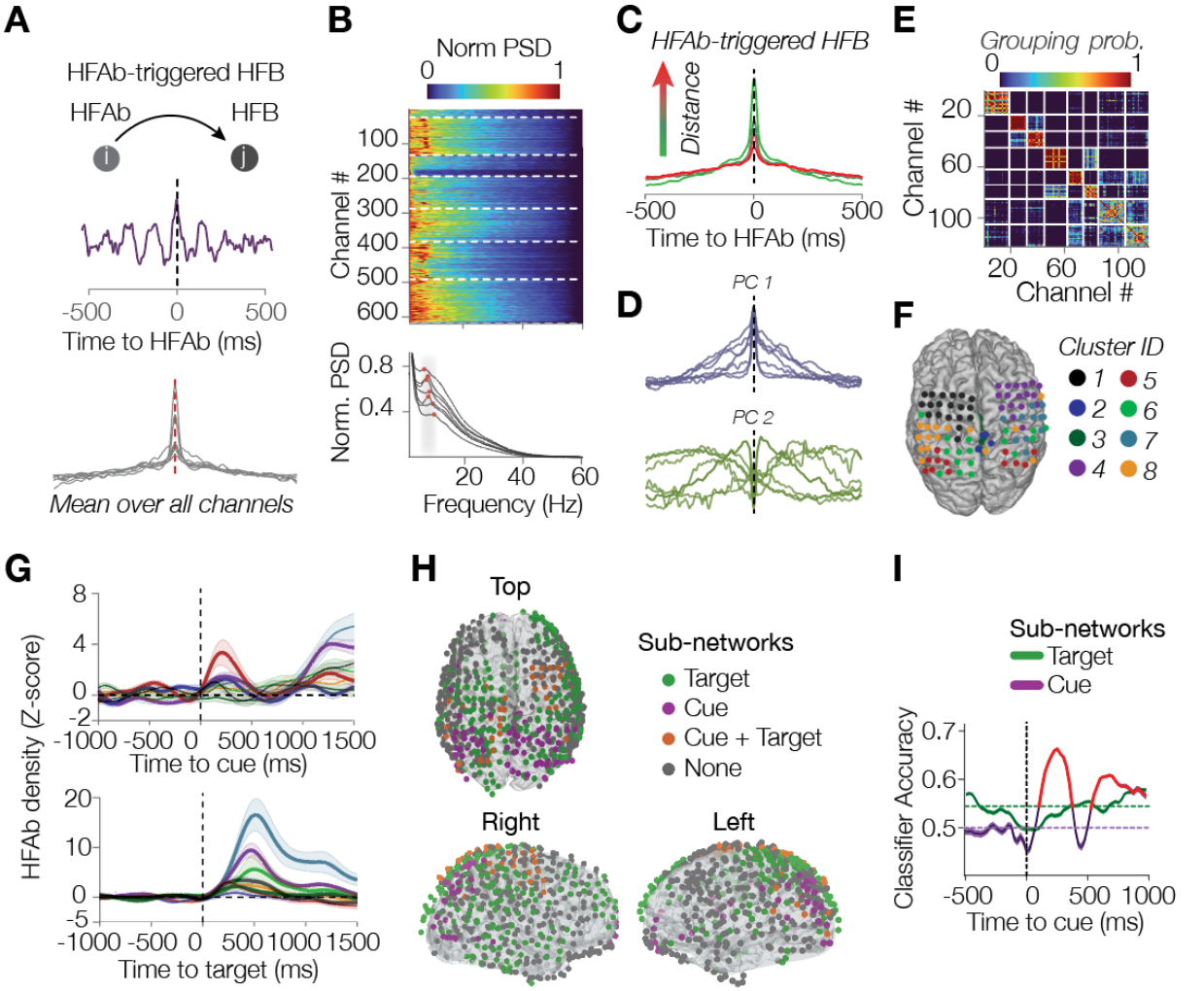

Fig. 3. Long-range coordination of HFAbs identifies functionally specialized subnetworks. **(A)** High frequency coordination was measured by calculating HFAb-triggered HFB between electrode pairs for HFAbs outside of cue/delay and target/response periods (top shows an electrode pair example, and bottom shows HFAb-triggered HFB averaged over all electrode pairs for individual subjects). **(B)** Normalized PSD over HFAb-triggered HFB for all electrodes (each electrode relative to the rest of the network; white dashed lines are the border between subjects)**.** **(C)** HFAb-triggered HFB for electrodes distanced in four quantiles, from green (short) to red (long). (**D**) The first two principal components of HFAb-triggered HFB for individual subjects. (**E**) A pair-wise grouping probability matrix for an individual example with an optimal number of eight clusters. Each element indicates the probability of two electrodes being grouped together across all random samples (white lines indicate cluster borders, clusters are ordered from top to bottom by their stability, see **Methods**). (**F**) Cluster topography for the K = 8 number of clusters for the individual subject shown in E. (**G**) Normalized burst densities around cue and target onsets averaged across electrodes within each cluster for the same subject as in E and F. (shaded error bars indicate the standard error of the mean; significant activations are indicated by thicker lines, $P<0.05$, Wilcoxon test). (**H**) Topographical organization of electrodes in clusters that show significant activation in response to cues and targets across all subjects (i.e., "cue-subnetworks" and "target-subnetworks"). (**I**) Classifier accuracy based on HFAb density around cue onset for

cue-subnetworks (purple) and target-subnetworks (green). Error bars indicate the standard error of the mean across all realizations and cross-validations. Red lines indicate significantly higher prediction accuracy than the baseline and chance level (binomial test, $P<0.05$, FDR corrected for dependent samples).

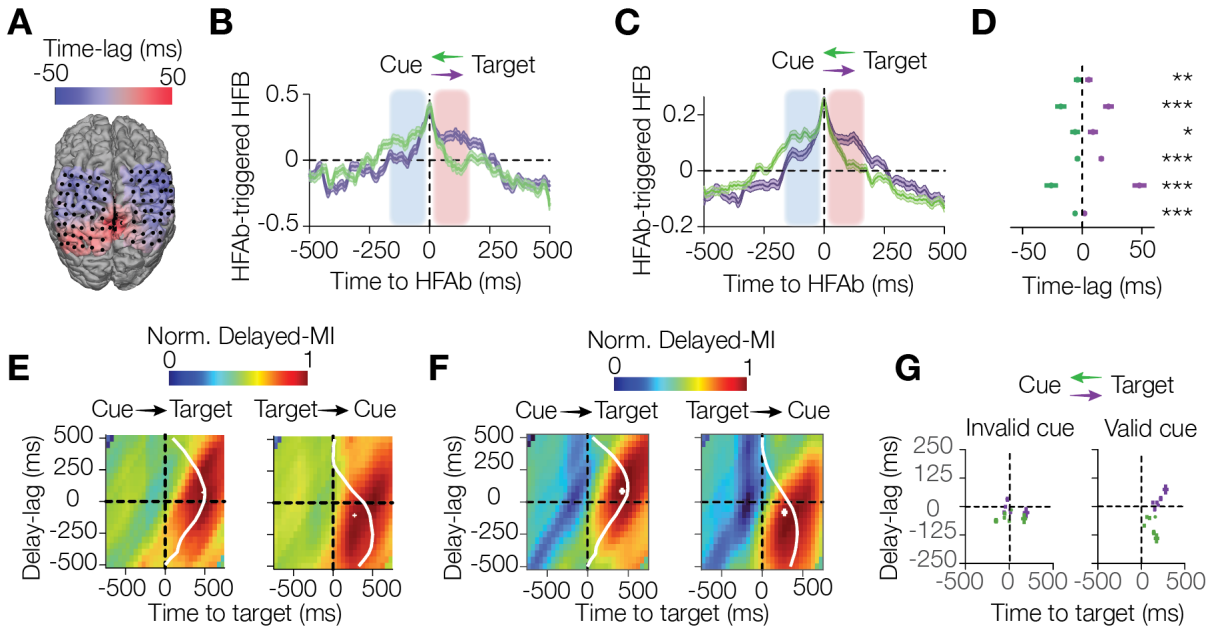

Fig. 4. Cue-subnetworks precede target-subnetworks during target processing. (A) An individual visualization example of the lead-lag patterns between electrodes in cue and target-subnetworks (across all cluster numbers) during the target processing period. The lead and lag temporal patterns are shown in a color gradient from red to blue. (**B**) Example of HFAb-triggered HFB for HFAbs during target processing, when HFB is measured in target-subnetworks relative to HFAbs in cue-subnetworks (purple) vs HFB is measured in cue-subnetworks relative to HFAbs in target-subnetworks (green). Red and blue shades denote significant difference between directions denoting a cue lead and a target lag respectively (Wilcoxon rank-sum test, $P<0.05$) (**C**) Group-level average of HFAb-triggered HFB, similar to B. (**D**) HFAb-triggered HFB median peak for electrode pairs corresponding to the same groups as in C (the Wilcoxon test was used to determine whether there was a difference in the distribution of peak positions between the two directions. Each row indicates the results for one individual. Error bars represent the standard error of the mean). (**E**) Heatmaps of normalized DMI values averaged across all members of the cue and target-subnetworks. The left panel shows DMI when the target-subnetwork is fixed, and the cue-subnetwork is shifted. The right panel shows DMI when the cue-subnetwork is fixed, and the target-subnetwork is shifted. The white line indicates the time-lag distribution of DMI peaks across electrode pairs. The cross signs indicate the median of DMI peak time-lags ± standard error. (**F**) Group average of DMI across all individuals, similar to E. (**G**) Comparisons of DMI peak distributions between the two opposite directions (green for shifting the cue-subnetwork and purple for shifting the target-subnetwork) for trials with valid (right) and invalid cues (left). Each individual is shown by a cross sign, which refers to the median ± standard error for DMI peaks across all electrode pairs between the two subnetworks.

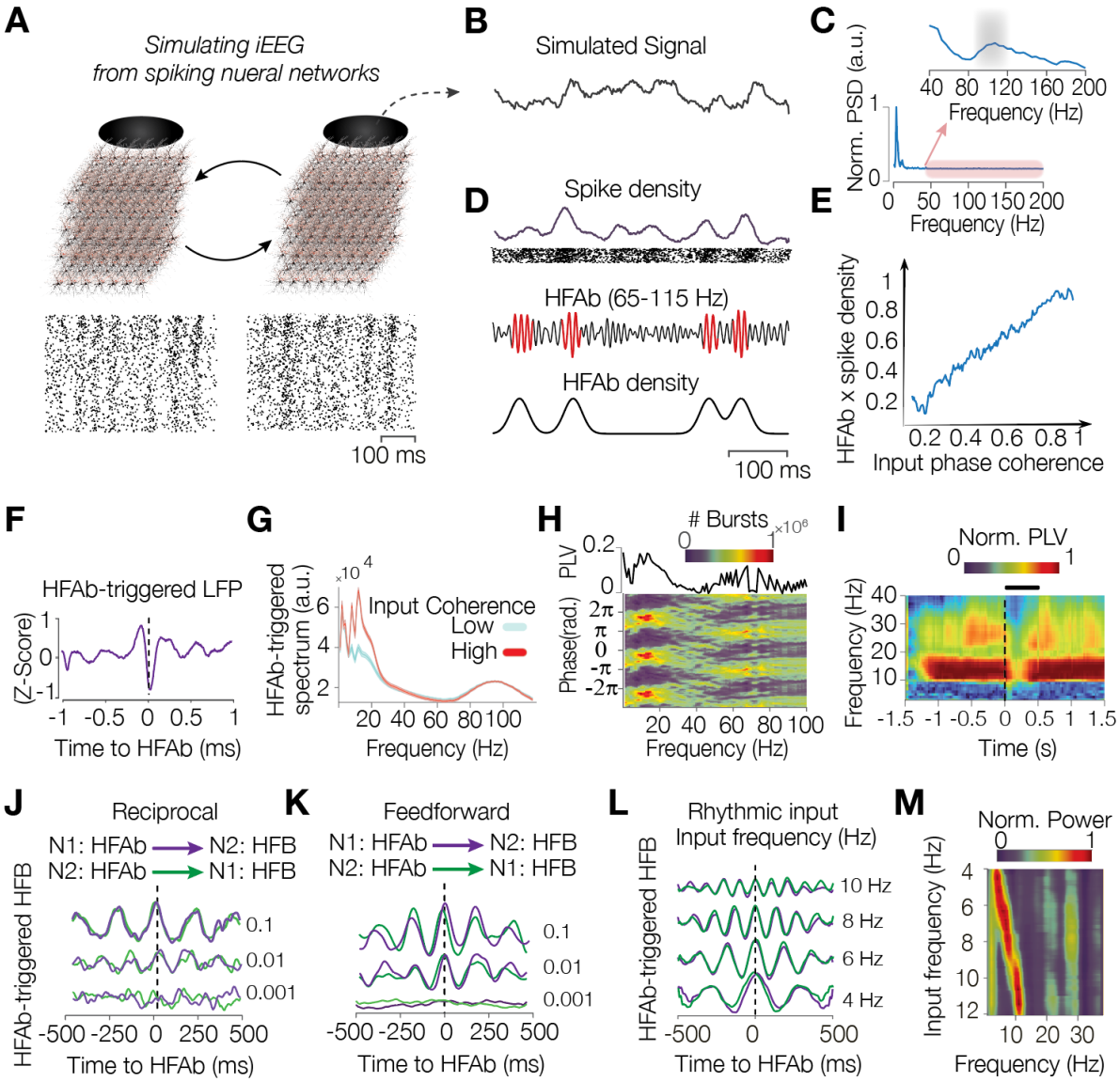

Fig. 5. Computational modeling of iEEG signals. (A) Two interconnected cubic networks of point source spiking neurons were simulated (bottom panels show raster plots for neurons in each network). A recording disk was implemented on top of each network to measure neural activity. (**B**) Example of simulated iEEG signals. (**C**) The power spectral density (PSD) of iEEG signals. (**D**) A single trial example of spike density and raster (top) detected HFAbs (middle, HFAbs are shown in red), and HFAb density (bottom). (**E**) HFAb density and spike density show linearly increasing correlations as input coherence increases. (**F**) HFAb-triggered LFP. (**G**) Cycle-balanced power spectrum triggered around HFAbs when the input to the network has high (red) or low coherence (cyan). (**H**) HFAb phase distribution at different frequencies. (**I**) The PLV of HFAbs to low frequencies after a transient input (thick black line) is fed to the network. (**J,K**) HFAb-triggered HFB between (**J**) reciprocally connected and (**K**) directional feedforward networks (connections from N1 to N2, see **Fig. S12E** for further details) with varying connectivity strengths (purple and green traces show HFAb-triggered HFB when bursts are extracted from N1 and N2, respectively). (**L**) HFAb-triggered HFB between disconnected networks with shared rhythmic inputs. (**M**) PSD over the HFAb-triggered HFB for rhythmic inputs of varying frequencies.

References

1. Y. B. Saalmann, I. N. Pigarev, T. R. Vidyasagar, Neural Mechanisms of Visual Attention: How Top-Down Feedback Highlights Relevant Locations. *Science* **316**, 1612–1615 (2007).

2. P. Fries, Neuronal Gamma-Band Synchronization as a Fundamental Process in Cortical Computation. *Annual Review of Neuroscience* **32**, 209–224 (2009).

3. G. G. Gregoriou, S. J. Gotts, H. Zhou, R. Desimone, High-Frequency, Long-Range Coupling Between Prefrontal and Visual Cortex During Attention. *Science* **324**, 1207–1210 (2009).

4. S. M. Szczepanski, N. E. Crone, R. A. Kuperman, K. I. Auguste, J. Parvizi, R. T. Knight, Dynamic Changes in Phase-Amplitude Coupling Facilitate Spatial Attention Control in Fronto-Parietal Cortex. *PLOS Biology* **12**, e1001936 (2014).

5. T. J. Buschman, S. Kastner, From Behavior to Neural Dynamics: An Integrated Theory of Attention. *Neuron* **88**, 127–144 (2015).

6. I. C. Fiebelkorn, S. Kastner, Functional Specialization in the Attention Network. *Annu Rev Psychol* **71**, 221–249 (2020).

7. K. Banaie Boroujeni, T. Womelsdorf, Routing states transition during oscillatory bursts and attentional selection. *Neuron*, doi: 10.1016/j.neuron.2023.06.012 (2023).

8. T. Womelsdorf, P. Fries, Neuronal coherence during selective attentional processing and sensory–motor integration. *Journal of Physiology-Paris* **100**, 182–193 (2006).

9. S. M. Doesburg, A. B. Roggeveen, K. Kitajo, L. M. Ward, Large-Scale Gamma-Band Phase Synchronization and Selective Attention. *Cerebral Cortex* **18**, 386–396 (2008).

10. P. Lakatos, G. Karmos, A. D. Mehta, I. Ulbert, C. E. Schroeder, Entrainment of Neuronal Oscillations as a Mechanism of Attentional Selection. *Science* **320**, 110–113 (2008).

11. M. Siegel, T. H. Donner, R. Oostenveld, P. Fries, A. K. Engel, Neuronal Synchronization along the Dorsal Visual Pathway Reflects the Focus of Spatial Attention. *Neuron* **60**, 709–719 (2008).

12. J. Hirvonen, S. Monto, S. H. Wang, J. M. Palva, S. Palva, Dynamic large-scale network synchronization from perception to action. *Network Neuroscience* **2**, 442–463 (2018).

13. J. Fan, B. D. McCandliss, J. Fossella, J. I. Flombaum, M. I. Posner, The activation of attentional networks. *NeuroImage* **26**, 471–479 (2005).

14. R. T. Canolty, K. Ganguly, S. W. Kennerley, C. F. Cadieu, K. Koepsell, J. D. Wallis, J. M. Carmena, Oscillatory phase coupling coordinates anatomically dispersed functional cell assemblies. *PNAS* **107**, 17356–17361 (2010).

15. U. Braun, A. Schäfer, H. Walter, S. Erk, N. Romanczuk-Seiferth, L. Haddad, J. I. Schweiger, O. Grimm, A. Heinz, H. Tost, A. Meyer-Lindenberg, D. S. Bassett, Dynamic reconfiguration of frontal brain networks during executive cognition in humans. *Proceedings of the National Academy of Sciences* **112**, 11678–11683 (2015).

16. D. S. Bassett, O. Sporns, Network neuroscience. *Nat Neurosci* **20**, 353–364 (2017).

17. A. Avena-Koenigsberger, B. Misic, O. Sporns, Communication dynamics in complex brain networks. *Nat Rev Neurosci* **19**, 17–33 (2018).

18. M. J. Brookes, J. R. Hale, J. M. Zumer, C. M. Stevenson, S. T. Francis, G. R. Barnes, J. P. Owen, P. G. Morris, S. S. Nagarajan, Measuring functional connectivity using MEG: Methodology and comparison with fcMRI. *NeuroImage* **56**, 1082–1104 (2011).

19. R. Hari, L. Parkkonen, The brain timewise: how timing shapes and supports brain function. *Philosophical Transactions of the Royal Society B: Biological Sciences* **370**, 20140170 (2015).

20. M. J. Higley, J. A. Cardin, Spatiotemporal dynamics in large-scale cortical networks. *Current Opinion in Neurobiology* **77**, 102627 (2022).

21. O. Jensen, L. L. Colgin, Cross-frequency coupling between neuronal oscillations. *Trends in Cognitive Sciences* **11**, 267–269 (2007).

22. R. T. Canolty, R. T. Knight, The functional role of cross-frequency coupling. *Trends in Cognitive Sciences* **14**, 506–515 (2010).

23. H. Jiang, A. Bahramisharif, M. A. J. van Gerven, O. Jensen, Measuring directionality between neuronal oscillations of different frequencies. *NeuroImage* **118**, 359–367 (2015).

24. B. Voytek, A. S. Kayser, D. Badre, D. Fegen, E. F. Chang, N. E. Crone, J. Parvizi, R. T. Knight, M. D'Esposito, Oscillatory dynamics coordinating human frontal networks in support of goal maintenance. *Nat Neurosci* **18**, 1318–1324 (2015).

25. M. Bonnefond, S. Kastner, O. Jensen, Communication between Brain Areas Based on Nested Oscillations. *eNeuro* **4**, ENEURO.0153-16.2017 (2017).

26. J. W. Y. Kam, J. J. Lin, A.-K. Solbakk, T. Endestad, P. G. Larsson, R. T. Knight, Default network and frontoparietal control network theta connectivity supports internal attention. *Nat Hum Behav* **3**, 1263–1270 (2019).

27. E. L. Johnson, J. J. Lin, D. King-Stephens, P. B. Weber, K. D. Laxer, I. Saez, F. Girgis, M. D'Esposito, R. T. Knight, D. Badre, A rapid theta network mechanism for flexible information encoding. *Nat Commun* **14**, 2872 (2023).

28. J.-P. Lachaux, N. Axmacher, F. Mormann, E. Halgren, N. E. Crone, High-frequency neural activity and human cognition: past, present and possible future of intracranial EEG research. *Prog Neurobiol* **98**, 279–301 (2012).

29. J. Parvizi, S. Kastner, Human Intracranial EEG: Promises and Limitations. *Nat Neurosci* **21**, 474–483 (2018).

30. S. Ray, J. H. R. Maunsell, Different Origins of Gamma Rhythm and High-Gamma Activity in Macaque Visual Cortex. *PLOS Biology* **9**, e1000610 (2011).

31. K. Banaie Boroujeni, P. Tiesinga, T. Womelsdorf, Adaptive spike-artifact removal from local field potentials uncovers prominent beta and gamma band neuronal synchronization. *Journal of Neuroscience Methods* **330**, 108485 (2020).

32. M. Leszczyński, A. Barczak, Y. Kajikawa, I. Ulbert, A. Y. Falchier, I. Tal, S. Haegens, L. Melloni, R. T. Knight, C. E. Schroeder, Dissociation of broadband high-frequency activity and neuronal firing in the neocortex. *Science Advances* **6**, eabb0977 (2020).

33. T. A. Zolnik, A. Bronec, A. Ross, M. Staab, R. N. S. Sachdev, Z. Molnár, B. J. Eickholt, M. E. Larkum, Layer 6b controls brain state via apical dendrites and the higher-order thalamocortical system. *Neuron* **112**, 805-820.e4 (2024).

34. S. Ray, E. Niebur, S. S. Hsiao, A. Sinai, N. E. Crone, High-frequency gamma activity (80-150 Hz) is increased in human cortex during selective attention. *Clin Neurophysiol* **119**, 116–133 (2008).

35. M. Haller, J. Case, N. E. Crone, E. F. Chang, D. King-Stephens, K. D. Laxer, P. B. Weber, J. Parvizi, R. T. Knight, A. Y. Shestyuk, Persistent neuronal activity in human prefrontal cortex links perception and action. *Nat Hum Behav* **2**, 80–91 (2018).

36. A. B. Martin, X. Yang, Y. B. Saalmann, L. Wang, A. Shestyuk, J. J. Lin, J. Parvizi, R. T. Knight, S. Kastner, Temporal Dynamics and Response Modulation across the Human Visual System in a Spatial Attention Task: An ECoG Study. *J. Neurosci.* **39**, 333–352 (2019).

37. C. Jacques, J. Jonas, S. Colnat-Coulbois, L. Maillard, B. Rossion, Low and high frequency intracranial neural signals match in the human associative cortex. *eLife* **11**, e76544 (2022).

38. G. Arnulfo, S. H. Wang, V. Myrov, B. Toselli, J. Hirvonen, M. M. Fato, L. Nobili, F. Cardinale, A. Rubino, A. Zhigalov, S. Palva, J. M. Palva, Long-range phase synchronization of high-frequency oscillations in human cortex. *Nat Commun* **11**, 5363 (2020).

39. N. Williams, S. H. Wang, G. Arnulfo, L. Nobili, S. Palva, J. M. Palva, Modules in connectomes of phase-synchronization comprise anatomically contiguous, functionally related regions. *NeuroImage* **272**, 120036 (2023).

40. J. C. Garrett, I. A. Verzhbinsky, E. Kaestner, C. Carlson, W. K. Doyle, O. Devinsky, T. Thesen, E. Halgren, Binding of cortical functional modules by synchronous high-frequency oscillations. *Nat Hum Behav*, 1–15 (2024).

41. R. F. Helfrich, I. C. Fiebelkorn, S. M. Szczepanski, J. J. Lin, J. Parvizi, R. T. Knight, S. Kastner, Neural Mechanisms of Sustained Attention Are Rhythmic. *Neuron* **99**, 854-865.e5 (2018).

42. E. M. Izhikevich, Which model to use for cortical spiking neurons? *IEEE Transactions on Neural Networks* **15**, 1063–1070 (2004).

43. A. Palmigiano, T. Geisel, F. Wolf, D. Battaglia, Flexible information routing by transient synchrony. *Nat Neurosci* **20**, 1014–1022 (2017).

44. M. Lundqvist, E. K. Miller, J. Nordmark, J. Liljefors, P. Herman, Beta: bursts of cognition. *Trends in Cognitive Sciences* **28**, 662–676 (2024).

45. L. L. Colgin, T. Denninger, M. Fyhn, T. Hafting, T. Bonnevie, O. Jensen, M.-B. Moser, E. I. Moser, Frequency of gamma oscillations routes flow of information in the hippocampus. *Nature* **462**, 353–357 (2009).

46. T. Akam, D. M. Kullmann, Oscillations and Filtering Networks Support Flexible Routing of Information. *Neuron* **67**, 308–320 (2010).

47. J. Yamamoto, J. Suh, D. Takeuchi, S. Tonegawa, Successful Execution of Working Memory Linked to Synchronized High-Frequency Gamma Oscillations. *Cell* **157**, 845–857 (2014).

48. G. Hahn, A. Ponce-Alvarez, G. Deco, A. Aertsen, A. Kumar, Portraits of communication in neuronal networks. *Nat Rev Neurosci* **20**, 117–127 (2019).

49. A. Fernandez-Ruiz, A. Sirota, V. Lopes-dos-Santos, D. Dupret, Over and above frequency: Gamma oscillations as units of neural circuit operations. *Neuron* **111**, 936–953 (2023).

50. P. König, A. K. Engel, W. Singer, Relation between oscillatory activity and long-range synchronization in cat visual cortex. *Proceedings of the National Academy of Sciences* **92**, 290–294 (1995).

51. P. R. Roelfsema, A. K. Engel, P. König, W. Singer, Visuomotor integration is associated with zero time-lag synchronization among cortical areas. *Nature* **385**, 157–161 (1997).

52. P. J. Uhlhaas, G. Pipa, B. Lima, L. Melloni, S. Neuenschwander, D. Nikolić, W. Singer, Neural Synchrony in Cortical Networks: History, Concept and Current Status. *Front Integr Neurosci* **3**, 17 (2009).

53. L. L. Gollo, C. Mirasso, A. E. P. Villa, Dynamic control for synchronization of separated cortical areas through thalamic relay. *NeuroImage* **52**, 947–955 (2010).

54. L. L. Gollo, C. R. Mirasso, M. Atienza, M. Crespo-Garcia, J. L. Cantero, Theta Band Zero-Lag Long-Range Cortical Synchronization via Hippocampal Dynamical Relaying. *PLOS ONE* **6**, e17756 (2011).

55. Y. B. Saalmann, S. Kastner, Cognitive and Perceptual Functions of the Visual Thalamus. *Neuron* **71**, 209–223 (2011).

56. N. K. Logothetis, O. Eschenko, Y. Murayama, M. Augath, T. Steudel, H. C. Evrard, M. Besserve, A. Oeltermann, Hippocampal–cortical interaction during periods of subcortical silence. *Nature* **491**, 547–553 (2012).

57. S. J. Sara, S. Bouret, Orienting and Reorienting: The Locus Coeruleus Mediates Cognition through Arousal. *Neuron* **76**, 130–141 (2012).

58. Y. B. Saalmann, M. A. Pinsk, L. Wang, X. Li, S. Kastner, The Pulvinar Regulates Information Transmission Between Cortical Areas Based on Attention Demands. *Science*, doi: 10.1126/science.1223082 (2012).

59. S. Vijayan, N. J. Kopell, Thalamic model of awake alpha oscillations and implications for stimulus processing. *Proceedings of the National Academy of Sciences* **109**, 18553–18558 (2012).

60. I. C. Fiebelkorn, M. A. Pinsk, S. Kastner, The mediodorsal pulvinar coordinates the macaque fronto-parietal network during rhythmic spatial attention. *Nat Commun* **10**, 215 (2019).

61. S. Kastner, I. C. Fiebelkorn, M. K. Eradath, Dynamic pulvino-cortical interactions in the primate attention network. *Current Opinion in Neurobiology* **65**, 10–19 (2020).

62. T. Menara, Y. Qin, D. S. Bassett, F. Pasqualetti, Relay Interactions Enable Remote Synchronization in Networks of Phase Oscillators. *IEEE Control Systems Letters* **6**, 500–505 (2022).

63. L. L. Gollo, C. Mirasso, O. Sporns, M. Breakspear, Mechanisms of Zero-Lag Synchronization in Cortical Motifs. *PLOS Computational Biology* **10**, e1003548 (2014).

64. T. A. Zolnik, J. Ledderose, M. Toumazou, T. Trimbuch, T. Oram, C. Rosenmund, B. J. Eickholt, R. N. S. Sachdev, M. E. Larkum, Layer 6b Is Driven by Intracortical Long-Range Projection Neurons. *Cell Reports* **30**, 3492-3505.e5 (2020).

65. S. M. Smith, P. T. Fox, K. L. Miller, D. C. Glahn, P. M. Fox, C. E. Mackay, N. Filippini, K. E. Watkins, R. Toro, A. R. Laird, C. F. Beckmann, Correspondence of the brain's functional architecture during activation and rest. *Proceedings of the National Academy of Sciences* **106**, 13040–13045 (2009).

66. A. R. Laird, S. B. Eickhoff, C. Rottschy, D. Bzdok, K. L. Ray, P. T. Fox, Networks of task co-activations. *NeuroImage* **80**, 505–514 (2013).

67. X.-J. Wang, G. R. Yang, A disinhibitory circuit motif and flexible information routing in the brain. *Current Opinion in Neurobiology* **49**, 75–83 (2018).

68. F. Battiston, G. Cencetti, I. Iacopini, V. Latora, M. Lucas, A. Patania, J.-G. Young, G. Petri, Networks beyond pairwise interactions: Structure and dynamics. *Physics Reports* **874**, 1–92 (2020).

69. S. L. Bressler, V. Menon, Large-scale brain networks in cognition: emerging methods and principles. *Trends in Cognitive Sciences* **14**, 277–290 (2010).

70. O. Jensen, B. Gips, T. O. Bergmann, M. Bonnefond, Temporal coding organized by coupled alpha and gamma oscillations prioritize visual processing. *Trends in Neurosciences* **37**, 357–369 (2014).

71. J. I. Chapeton, R. Haque, J. H. Wittig, S. K. Inati, K. A. Zaghloul, Large-Scale Communication in the Human Brain Is Rhythmically Modulated through Alpha Coherence. *Current Biology* **29**, 2801-2811.e5 (2019).

72. K. D. Harris, A. Thiele, Cortical state and attention. *Nat Rev Neurosci* **12**, 509–523 (2011).

73. R. Gast, S. A. Solla, A. Kennedy, Neural heterogeneity controls computations in spiking neural networks. *Proceedings of the National Academy of Sciences* **121**, e2311885121 (2024).

74. S. Hanslmayr, T. Staudigl, M.-C. Fellner, Oscillatory power decreases and long-term memory: the information via desynchronization hypothesis. *Front. Hum. Neurosci.* **6** (2012).

75. S. Hanslmayr, B. P. Staresina, H. Bowman, Oscillations and Episodic Memory: Addressing the Synchronization/Desynchronization Conundrum. *Trends in Neurosciences* **39**, 16–25 (2016).

76. C. B. Beaman, S. L. Eagleman, V. Dragoi, Sensory coding accuracy and perceptual performance are improved during the desynchronized cortical state. *Nat Commun* **8**, 1308 (2017).

77. A. Nandy, J. J. Nassi, M. P. Jadi, J. Reynolds, Optogenetically induced low-frequency correlations impair perception. *eLife* **8**, e35123 (2019).

78. N. Weisz, N. G. Kraft, G. Demarchi, Auditory cortical alpha/beta desynchronization prioritizes the representation of memory items during a retention period. *eLife* **9**, e55508 (2020).

79. R. Egly, J. Driver, R. D. Rafal, Shifting visual attention between objects and locations: Evidence from normal and parietal lesion subjects. *Journal of Experimental Psychology: General* **123**, 161–177 (1994).

80. I. C. Fiebelkorn, Y. B. Saalmann, S. Kastner, Rhythmic Sampling within and between Objects despite Sustained Attention at a Cued Location. *Current Biology* **23**, 2553–2558 (2013).

81. B. Boashash, “Estimating and Interpreting the Instantaneous Frequency of a Signal – Part 1: Fundamentals” in *Proceedings of the Ieee* (1992), pp. 520–538.

82. M. R. H. Hill, I. Fried, C. Koch, Quantification and classification of neuronal responses in kernel-smoothed peristimulus time histograms. *Journal of Neurophysiology* **113**, 1260–1274 (2015).

83. O. J. Dunn, Multiple Comparisons among Means. *Journal of the American Statistical Association* **56**, 52–64 (1961).

84. Y. Benjamini, D. Yekutieli, False Discovery Rate–Adjusted Multiple Confidence Intervals for Selected Parameters. *Journal of the American Statistical Association* **100**, 71–81 (2005).

85. N. I. Fisher, *Statistical Analysis of Circular Data* (Cambridge University Press, 1995).

86. G. W. Milligan, M. C. Cooper, An examination of procedures for determining the number of clusters in a data set. *Psychometrika* **50**, 159–179 (1985).

87. A. K. Jain, R. C. Dubes, *Algorithms for Clustering Data* (Prentice-Hall, Inc., USA, 1988).

88. M. Halkidi, Y. Batistakis, M. Vazirgiannis, On Clustering Validation Techniques. *Journal of Intelligent Information Systems* **17**, 107–145 (2001).

89. L. Vendramin, R. J. G. B. Campello, E. R. Hruschka, Relative clustering validity criteria: A comparative overview. *Statistical Analysis and Data Mining: The ASA Data Science Journal* **3**, 209–235 (2010).

90. D. Freedman, P. Diaconis, On the histogram as a density estimator:L2 theory. *Z. Wahrscheinlichkeitstheorie verw Gebiete* **57**, 453–476 (1981).

91. Y. N. Billeh, B. Cai, S. L. Gratiy, K. Dai, R. Iyer, N. W. Gouwens, R. Abbasi-Asl, X. Jia, J. H. Siegle, S. R. Olsen, C. Koch, S. Mihalas, A. Arkhipov, Systematic Integration of Structural and Functional Data into Multi-scale Models of Mouse Primary Visual Cortex. *Neuron* **106**, 388-403.e18 (2020).

92. T. C. Potjans, M. Diesmann, The Cell-Type Specific Cortical Microcircuit: Relating Structure and Activity in a Full-Scale Spiking Network Model. *Cerebral Cortex* **24**, 785–806 (2014).

93. J. Barral, A. D Reyes, Synaptic scaling rule preserves excitatory–inhibitory balance and salient neuronal network dynamics. *Nat Neurosci* **19**, 1690–1696 (2016).

94. E. M. Izhikevich, Simple model of spiking neurons. *IEEE Transactions on Neural Networks* **14**, 1569–1572 (2003).

95. C. K. Pfeffer, M. Xue, M. He, Z. J. Huang, M. Scanziani, Inhibition of inhibition in visual cortex: the logic of connections between molecularly distinct interneurons. *Nat Neurosci* **16**, 1068–1076 (2013).

96. M. M. Karnani, J. Jackson, I. Ayzenshtat, J. Tucciarone, K. Manoocheri, W. G. Snider, R. Yuste, Cooperative Subnetworks of Molecularly Similar Interneurons in Mouse Neocortex. *Neuron* **90**, 86–100 (2016).

97. M. Medalla, J. P. Gilman, J.-Y. Wang, J. I. Luebke, Strength and Diversity of Inhibitory Signaling Differentiates Primate Anterior Cingulate from Lateral Prefrontal Cortex. *J. Neurosci.* **37**, 4717–4734 (2017).

98. J. P. Gilman, M. Medalla, J. I. Luebke, Area-Specific Features of Pyramidal Neurons—a Comparative Study in Mouse and Rhesus Monkey. *Cerebral Cortex* **27**, 2078–2094 (2017).

99. M. Medalla, J. I. Luebke, Diversity of Glutamatergic Synaptic Strength in Lateral Prefrontal versus Primary Visual Cortices in the Rhesus Monkey. *J. Neurosci.* **35**, 112–127 (2015).

100. J. M. Amatrudo, C. M. Weaver, J. L. Crimins, P. R. Hof, D. L. Rosene, J. I. Luebke, Influence of Highly Distinctive Structural Properties on the Excitability of Pyramidal Neurons in Monkey Visual and Prefrontal Cortices. *J. Neurosci.* **32**, 13644–13660 (2012).

101. A. Roxin, N. Brunel, D. Hansel, G. Mongillo, C. van Vreeswijk, On the Distribution of Firing Rates in Networks of Cortical Neurons. *J. Neurosci.* **31**, 16217–16226 (2011).

102. J. Milstein, F. Mormann, I. Fried, C. Koch, Neuronal Shot Noise and Brownian 1/f2 Behavior in the Local Field Potential. *PLOS ONE* **4**, e4338 (2009).

103. C. Bédard, H. Kröger, A. Destexhe, Modeling Extracellular Field Potentials and the Frequency-Filtering Properties of Extracellular Space. *Biophysical Journal* **86**, 1829–1842 (2004).